Aggregation and breakup of colloidal particle aggregates in shear flow: A combined Monte Carlo - Stokesian dynamics approach

(Article begins on next page)

12 June 2023

Aggregation and breakup of colloidal particle aggregates in shear flow: a combined Monte Carlo - Stokesian dynamics approach

Graziano Frungieri[a,1,*], Marco Vanni[a,2]

[a]*Department of Applied Science and Techonology, Politecnico di Torino, Corso Duca degli Abruzzi 24, Torino, Italy*

Abstract

A method for the simulation of aggregation and breakup processes in colloidal particle suspensions is presented. The method combines a Monte Carlo algorithm to determine, on the basis of probabilistic considerations, the sequence of aggregation and breakup events, and a Discrete Element Method, built in the framework of Stokesian dynamics and contact mechanics, to accurately reproduce them. Liquid-solid suspensions subject to a uniform shear stress are investigated. The model is seen to be able to reproduce the typical dynamic steady state which is observed in colloidal suspensions under severe shearing, in which the effects of aggregation and breakup balance each other. The structural properties of the aggregates and the dynamics of the aggregation and breakup phenomena are characterized in detail. Both fragmentation and erosion are seen to contribute to the breakup process, which is characterized by an exponent similar to the one reported in the literature for compact clusters.

Keywords: Colloidal suspensions, aggregation, breakup, shear flow, discrete element method, Monte Carlo

---

*Corresponding author
  Email address: `graziano.frungieri@polito.it` (Graziano Frungieri)
  [1]graziano.frungieri@polito.it, Tel: +39 0110904593
  [2]marco.vanni@polito.it

1. Introduction

The dynamics of a destabilized colloidal suspension subject to strong mechanical agitation initially proceeds through the shear-induced aggregation of the primary particles of the disperse phase. Subsequently, when the size of the aggregates becomes so large that the hydrodynamic stress acting on them exceeds their cohesive strength, the biggest clusters start breaking up and, in the end, a dynamic steady state condition may be reached, in which the properties of the suspension do not change any longer and the effects of aggregation and breakup balance each other. The evolution toward this dynamic steady state is typical of colloidal processes conducted under intense stirring and it was evidenced experimentally by a number of researchers, both under simple laminar flow configurations [1–5] and in complex turbulent flow fields [6–9]. This type of conditions, in which shear-induced aggregation and breakup act simultaneously, are usually achieved in suspensions at large Péclet number, where the role of Brownian motion is negligible in comparison to the effects of the shear flow. Such situations are relatively common in the colloidal domain and may occur in flocculation [10–13], polymer processing and compounding [14, 15], flow of complex fluids [16–19]. Even in the production of micro and nanoparticles by wet route, shear-induced aggregation and breakup may play a significant role in determining the properties of the product, although in parallel with the nucleation and growth of the particles, and the Brownian aggregation at the smallest scales [20].

The dynamics of colloidal systems subject to aggregation and breakup is usually calculated by solving the Population Balance Equation [21] (PBE), a differential equation that describes statistically the change of the properties of a population of particles (e.g., size, mass, aspect ratio, composition, ...). The approach dates back to the analysis of fast coagulation by Smoluchowski, where the investigated property was the number of primary particles of each aggregate. Subsequently, the approach was made more general and applicable to any of the properties of a population of particles. In this general form the PBE is

2

largely used to describe aggregation/breakup processes in colloidal dispersions. In most cases a single internal variable is considered (usually particle volume in aggregation-breakup systems) [22–26] and, indeed, this is sufficient if the information on particle morphology is not required and all the phenomena of interest involve only volume or size. However, in some cases one may need other variables to describe the internal structure of the aggregates and a number of bivariate PBE was indeed applied to the study of aggregation and breakup. In such cases, the most common choice of internal variables is particle volume (or, equivalently, number of primary particles of the aggregate) and fractal dimension [27–29], or particle size and fractal dimension [30, 31].

The population balance method has a relatively small computational cost, but it is not completely predictive, in that it needs models for the rates of aggregation and breakup, and for the change of shape and morphology of the aggregates. Various approaches can be used to infer such information. Bäbler and coworkers, for instance, measured the breakup rate in a homogeneous isotropic turbulence by following aggregates along Lagrangian paths and assuming that breakup occurs instantaneously as soon as the aggregates experience a hydrodynamic stress exceeding a critical threshold value [32, 33]. Zaccone et al. [34] used a crack propagation model to derive a scaling law between size and critical stress for varying aggregate fractal dimension. Drossinos et al. [35] developed an algorithm for random binary fragmentation, by which they estimated breakup frequencies and the size distribution of the daughter particles.

A more predictive description of the processes of aggregation and fragmentation can be obtained from Discrete Element Methods (DEMs), in which the trajectory of each primary particle of the suspension is computed by solving its equation of motion and considering all the forces acting on it (including fluid dynamic, contact and colloidal interactions). When this method is applied to colloidal suspensions, however, the implementation of fluid dynamic interaction may become critical, because of its complex and long-ranged nature, which is very different from the short-ranged contact forces typical of the granular solids for which DEM codes were originally developed. For this reason the use of

3

DEMs for the study of colloidal processes is normally based on drastic simplifications of the fluid dynamic interaction. The most common approach is the *free draining approximation*, in which each particle interacts with the sur-

rounding liquid as it were alone in the system [36–40], thus neglecting all fluid mediated particle-particle interactions. These, however, were seen to strongly influence aggregation efficiencies [10, 41–43], stress distribution inside the aggregates [15, 44, 45], and consequently their mode of aggregating, [13, 46] breaking up and restructuring [47–49].

The aim of this work is to present and apply a method that takes into account all the relevant particle-particle interaction and which is able to simulate in detail the dynamics of a colloidal suspension at a reasonable computational cost. We investigate the evolution of a large population of colloidal particles suspended in a liquid medium and subject to a uniform shear flow. To circumvent the problem of the exceedingly high computational cost of the DEM simulations, the developed method combines a Monte Carlo approach to determine, on the basis of probabilistic considerations, the sequence of aggregation and breakup events and the clusters involved, and a Discrete Element Method, built in the framework of Stokesian Dynamics, to accurately reproduce the event. In this way the DEM simulations only involve the relatively small number of primary particles composing the two clusters involved in an event, thus allowing us to avoid to track simultaneously all the primary particles of the population throughout the process. The DEM model is able to evaluate the fluid-dynamic stress acting on each monomer and to describe properly the inter-particle interactions that arise from van der Waals attraction and elastic deformation at the contact between the solid surfaces.

A preliminary version of the method was used previously to investigate a purely aggregating system [46]. However, that work was focused mostly on the outcomes of the model, whereas the approach and the model behind were not described in detail. In this work the method is presented in depth and we report the results of simulations for suspensions in which aggregation and breakup occur simultaneously, with a particular regard to the determination

4

of size distribution and morphologies of aggregates. As discussed before, our approach is quite different from the other ones reported in the literature for this type of problems since it makes it possible to model with great accuracy the evolution of a large population of aggregates. So far, in fact, Stokesian dynamics has been used solely to model events involving one or two aggregates at most, whereas large populations have been generally described by adopting simplified fluid dynamics models.

2. Methods

The evolution of a colloidal suspension is determined by a sequence of distinct events of aggregation and breakup. In a uniform shear flow all such events are driven by encounters between the suspended particles, that is, situations where two particles approach so closely that the probability of collision becomes significant. (In the following we will use the term *particle* to identify any entity capable of moving independently in the fluid. Consequently, this term includes both aggregates and free primary particles, i.e., primary particles which do not belong to any aggregate). If an encounter actually ends up in the collision of the two particles and the attractive colloidal forces are strong enough to keep them in contact, the process leads to the formation of a single stable daughter aggregate, and it will be referred to as an *aggregation* event. If the formed aggregate is very large, the accumulation of hydrodynamic stresses on its structure may become so intense to exceed the cohesive forces acting between primary particles in some points of the structure and the aggregate may split into two or more fragments [44, 50]. Since the dynamics of breakup is fast when the critical size is exceeded [51], in this case we describe the global process (*i.e.*, the sequence of aggregation and rupture) as a single *breakup* event. Finally, the situation in which an encounter does not end up in a collision and the two particles preserve their individuality will be referred to as a *missed collision* event. It is worth observing that the coupling between rupture and aggregation in a single event is strictly related to the assumption of a uniform shear flow. In non-uniform

5

flow fields breakup may occur independently of aggregation whenever a particle moves from a region of low strain rate to a region of higher strain rate.

In the present work the dynamics of colloidal suspensions subject to a uniform shear flow is simulated by an event-driven, rejection-free Monte Carlo algorithm [52], in which the evolution of the particulate system is simulated by creating an artificial realization of the studied process through the numerical generation of a sequence of random events, which obeys the same statistical laws as the physical system [53]. While the expected frequency of encounters can be evaluated a priori, their outcome (aggregation, breakup or missed collision) is established by resorting to an accurate DEM simulation, by which the motion of all the primary particles composing the involved aggregates is tracked. The DEM also provides detailed information on the geometry and structure of the aggregates at the end of the encounter. We applied this model on dilute suspensions: in this condition it is reasonable to consider encounters as binary events, i.e., events involving only two aggregates at once.

In order to deal with a reasonably small population of particles, only a small portion ΔV of the volume of the system is actually simulated, assuming that the behaviour of the particles in this subvolume replicates the statistical features of the real suspension as a whole, as originally suggested by Liffman [54]. The size of the subvolume can be changed during the simulation, in order to have a statistically significant number of particles at any time of the process. A simple shear flow was assumed to act on the suspension with constant and uniform rate $\dot{\gamma} = \frac{\mathrm{d}u_z}{\mathrm{d}y}$. The Brownian motion of the particles was neglected, since the process occurs at high Péclet numbers (Pe $= 6\pi\mu a^3\dot{\gamma}/k_B T > 10^5$) where convection is largely predominant over the thermal motion of the particles.

2.1. Monte Carlo algorithm

To tune the Monte Carlo algorithm, a model is needed to evaluate the pair encounter frequency between the simulated particles, i.e., the probability for a certain couple of particles to meet each other in the suspension. To this purpose, a precise characterization of an encounter is needed.

6

Figure 1 shows two aggregates, i and j, approaching each other in a uniform shear flow. The aggregates are made of primary particles with radius a. The size of an aggregate is characterized by its external radius R, which is the maximum distance between the surface of a primary particle and the center of mass of the aggregate: $R = \max_k(|\mathbf{x}_k - \mathbf{x}_{cm}|) + a$, where $|\mathbf{x}_k - \mathbf{x}_{cm}|$ is the distance of the k-th primary particle from the center of mass of the aggregate. If the two aggregates were solid spheres of radii R_i and R_j and no colloidal force or lubrication interaction acted between them (as in the original approach by Smoluchowski for shear coagulation [55]), particle j would eventually collide with particle i if its center of mass crosses the circular collision cross section of radius $(R_i + R_j)$, which is shown in grey in Figure 1 and is located on a plane of constant z far upstream of particle i. The expected rate for this type of collision in a volume ΔV is:

$$f_{ij} = \frac{4}{3}\dot{\gamma}\left(R_i + R_j\right)^3 c_i c_j \Delta V \tag{1}$$

where c_i and c_j are the number concentrations of particles i and j, both equal to $1/\Delta V$ because only one i-particle and one j-particle are present in the subvolume. In our system, however, the irregular shape of the aggregates and the presence of hydrodynamic interactions strongly reduces the probability of contact. Hence, crossing the cross-section of size $(R_i + R_j)$ does not necessarily lead to a collision between aggregates i and j. This is why the rate given by Eq. (1) is not the actual collision frequency for our system, but it is instead regarded as the frequency at which a close encounter is expected between i and j. Such an encounter can subsequently evolve in a missed collision, an aggregation or a breakup event.

[Figure 1 about here.]

By substituting the values of c_i and c_j, the encounter frequency between i and j-particles becomes as follows:

$$f_{ij} = \frac{4}{3}\dot{\gamma}\frac{\left(R_i + R_j\right)^3}{\Delta V} \tag{2}$$

Differently from the analysis by Smoluchowski, we used this information to model solely the encounter frequency between pairs of clusters, whereas the actual outcome of a close encounter is ascertained from the detailed DEM simulation described in the following section.

The total encounter frequency for N_a suspended aggregates contained in the subvolume ΔV is given by:

$$f_{\text{tot}} = \sum_{i}^{N_a} \sum_{j=i+1}^{N_a-1} f_{ij} \tag{3}$$

We used this information to estimate the time interval elapsing between two subsequent encounters. This time interval can be regarded as an interval of quiescence (IQ), i.e., as a waiting time during which no encounter occurs and the population remains unchanged [56]. If an encounter occurred at time t_0, the probability for a new encounter to take place at time $t = t_0 + IQ$ is given by:

$$\Pr\left(\text{IQ}\right) = 1 - e^{-f_{\text{tot}}\text{IQ}} \tag{4}$$

Since the phenomena are stochastic, the interval of quiescence can be sampled from a random variable with the cumulative distribution function given by Eq. (4).

Once determined the time at which the new encounter occurs, the Monte Carlo method has to select the aggregates involved. The probability of occurrence of a generic encounter k involving aggregates i and j is:

$$\Pr_k = f_{ij}/f_{\text{tot}} \tag{5}$$

[Figure 2 about here.]

From an ordered list of all possible encounters the algorithm chooses the event with index q, which satisfies the following relationship:

$$\sum_{k=1}^{q-1} \Pr_k < \xi < \sum_{k=1}^{q} \Pr_k \tag{6}$$

where ξ is a random number sampled from a uniform distribution between 0 and 1. Figure 2 shows the method for a small sample population made of 4

8

aggregates. This technique, usually referred to as inversion method [57], was preferred over other approaches, such as the acceptance-rejection method [58, 59], which could result in a very large number of attempts before a pair of aggregates is sampled.

The subsequent step of the method is the simulation of the encounter between the two sampled aggregates by means of a Discrete Element Method based on Stokesian dynamics. However, before executing the DEM simulation, the initial spatial coordinates of the particles have to be prescribed (Figure 1). The center of mass of aggregate i is placed in the origin of the reference system; aggregate j is instead located far upstream from aggregate i and inside the encounter cross section. Its exact position is determined on the basis of statistical considerations. Far from aggregate i the translational velocity of aggregate j equals the undisturbed fluid velocity, $u_z = \dot{\gamma}y$, which is linearly increasing with y and independent of x. The distribution of the probability for particle j of crossing the encounter cross section at coordinates (x, y) should reproduce such profiles. As a consequence, if we examine the square of size $(R_i + R_j)$ enclosing the encounter cross section (graph a of Figure 3), the initial coordinates (x_j^0, y_j^0) for aggregate j can be found by picking up a random number from a uniform probability distribution for x (graph b of Figure 3) and a linear probability distribution for y (graph c), respectively. The sampling must be repeated until the condition $\sqrt{\left(x_j^0\right)^2 + \left(y_j^0\right)^2} \leq (R_i + R_j)$ is satisfied, in order to ensure that the center of mass of aggregate j is located inside the encounter cross section. The z_j^0-coordinate was set equal to $\pm 5 (R_i + R_j)$, with the $\pm$ sign determined according to the sign of the y coordinate. At this distance the hydrodynamic interactions acting between the two approaching aggregates are not significant and we can reasonably assume that, in this initial configuration, the aggregates have the same velocity as the undisturbed fluid.

[Figure 3 about here.]

The advantage of combining the DEM model with the Monte Carlo method stays in the possibility of tracking the motion of every primary particle of the

9

approaching aggregates, thus allowing us to establish the effective outcome of the encounter event and the accurate geometry of the resulting aggregate/s.

The detailed description of the DEM and its features is postponed to the next section. Here it suffices to say that an encounter may lead to three qualitatively different outcomes:

- *missed collision*: a close pass of the two aggregates without an actual collision and with no change of the number of primary particles composing the two aggregates;

- *aggregation*: the two aggregates collide forming one stable larger aggregate;

- *breakup*: the generation of new fragments from the encountering aggregates.

Any aggregation event causes the net loss of one aggregate from the population, since the two parent aggregates are substituted by the daughter one. On the contrary, a breakup event may result either in no change of the total number of aggregates, if only two fragments are produced after a collision occurred, or in an increase of the number of particles, if three or more fragments are generated. As described in more detail in the subsequent sections, the DEM simulation lasts for a time long enough for breakup to occur according to the criterion by Harshe and Lattuada [51], which is valid when the applied viscous stress exceeds the cohesive strength of the particles. When the viscous stress is slightly smaller than the cohesive strength, a slow process of deterioration of the structure may take place, which gradually reduces the strength of the aggregate and may end up with its rupture [60]. Such a process is slow and is not captured by our DEM simulation. However, it affects only the few aggregates with size very close to the critical one and hence it is unlikely to influence significantly the statistics of the whole population.

In all cases, even if no collision has occurred, the fluid stresses exerted by the fluid can rearrange the positions of the primary particles, deforming the

10

overall morphology of the aggregates. Although such a rearrangement takes place during the whole life of an aggregate, for the sake of simplicity, we take this effect into account only during encounters, assuming that the geometry of the aggregates remains frozen during the rest of their life.

Due to the changes in geometry, the birth of new aggregates and the death of old ones originated by the aforementioned events, the encounter frequencies involving any of the aggregates returning from the DEM simulation need to be corrected or calculated ex-novo, updating the frequencies f_{ij}.

[Figure 4 about here.]

A flow-chart of the method is reported in Figure 4. After setting up the initial population of particles (a monodisperse population of identical primary particles in the results reported herein), the frequency table f_{ij} for all possible encounters is calculated from Eq. (2). At this point the interval of quiescence Δt after which a new encounter occurs is sampled randomly from the distribution of Eq. (4). The two aggregates involved in the encounter are identified on the basis of the encounter probability table f_{ij}, and their position at the initial time of the encounter is set accordingly to the far field fluid velocity distribution, as described before. In addition, the two aggregates are given a random orientation about their center of mass, to take into account also the complex rotational motion they underwent before the encounter. The encounter is simulated accurately through the DEM and, on the basis of the outcome of the event, the population is updated. At this point, the process can be restarted with the new population, until the prescribed number of events has been simulated.

At the beginning of the process, when the population is made mainly of primary particles or very small aggregates, aggregation largely prevails over breakup, and the large reduction of the number of aggregates could prevent the simulation from returning statistically reliable results. Several approaches have been used to circumvent this problem, preserving statistical robustness [54, 58]. In this work we decided to double the volume of the subsystem whenever the number of simulated aggregates fell below a critical threshold. An exact copy of

11

the population was added to the system, thus preserving both number density and particle size distribution. The critical threshold was set equal to 75% of the initial number of particles.

2.2. DEM simulation of the encounters

The basic idea behind our Discrete Element Method is that aggregates are composed by distinct elements, equally-sized spherical primary particles, kept together via colloidal interactions and subject to the hydrodynamic stresses exerted by the moving fluid. By modelling all these interactions and solving the equations of motion, we track the trajectory of each individual primary particle and, consequently, predict the dynamics of the aggregates. In the present work hydrodynamic interactions are modelled by Stokesian dynamics, whereas direct particle-particle interaction results solely from the van der Waals attraction and the elastic forces due to the deformation of the contacts. No other source of interparticle forces (e.g., double layer, adsorbed polymers, solid friction, ...) is here considered.

2.2.1. Hydrodynamic interaction

Stokesian dynamics in its FTS (force, torque, stresslet) formulation was adopted to evaluate the hydrodynamic interactions among all the primary particles of the two approaching aggregates. Stokesian dynamics, relying on the linearity of the Stokes equation, is able to accurately count for all the hydrodynamic interactions, including particle-fluid and fluid mediated particle-particle interactions. It operates by relating the hydrodynamic force, torque and stresslet acting on the particles to their relative velocity with respect to the fluid [61, 62].

For the simple shear flow $\mathbf{u}^\infty(\mathbf{r}) = \dot{\gamma}y\mathbf{e}_z$, with $\mathbf{e}_z$ being the unit vector aligned to the z direction, the undisturbed velocity of the medium $\mathbf{u}^\infty$ in any point $\mathbf{r} = (x, y, z)$ can be expressed as the superposition of a pure rotating flow field with angular velocity $\boldsymbol{\omega}^\infty$ and a pure straining motion with deformation

12

rate tensor $\mathbf{E}^\infty$:

$$\mathbf{u}^\infty\left(\mathbf{r}\right) = \boldsymbol{\omega}^\infty \times \mathbf{r} + \mathbf{E}^\infty \cdot \mathbf{r}, \tag{7}$$

where the only non-zero elements are $\omega_x^\infty = \dot{\gamma}/2$ for the angular velocity and $E_{yz}^\infty = E_{zy}^\infty = \dot{\gamma}/2$ for the deformation rate. The velocity of each one of the N primary particles can be obtained by solving the following linear system:

$$\left[\mathcal{R}\right] \cdot \left\{ \begin{array}{c} \mathbf{u}^{(1)} - \mathbf{u}^\infty\left(\mathbf{r}_1\right) \\ \vdots \\ \mathbf{u}^{(N)} - \mathbf{u}^\infty\left(\mathbf{r}_N\right) \\ \boldsymbol{\omega}^{(1)} - \boldsymbol{\omega}^\infty \\ \vdots \\ \boldsymbol{\omega}^{(N)} - \boldsymbol{\omega}^\infty \\ -\mathbf{E}^\infty \\ \vdots \\ -\mathbf{E}^\infty \end{array} \right\} = - \left\{ \begin{array}{c} \mathbf{F}_{\mathrm{H}}^{(1)} \\ \vdots \\ \mathbf{F}_{\mathrm{H}}^{(N)} \\ \mathbf{T}_{\mathrm{H}}^{(1)} \\ \vdots \\ \mathbf{T}_{\mathrm{H}}^{(N)} \\ \mathbf{S}_{\mathrm{H}}^{(1)} \\ \vdots \\ \mathbf{S}_{\mathrm{H}}^{(N)} \end{array} \right\} \tag{8}$$

where the vectors $\mathbf{u}^{(\alpha)} = \left(u_x^{(\alpha)}, u_y^{(\alpha)}, u_z^{(\alpha)}\right)$ and $\boldsymbol{\omega}^{(\alpha)} = \left(\omega_x^{(\alpha)}, \omega_y^{(\alpha)}, \omega_z^{(\alpha)}\right)$ are respectively the linear and angular velocity of the α-th primary particle, whereas $\mathbf{u}^\infty\left(\mathbf{r}_\alpha\right)$ is the velocity of the undisturbed flow field at the center of the α-th primary particle. The undisturbed fluid angular velocity, $\boldsymbol{\omega}^\infty$, does not depend on the spatial position in the investigated uniform shear flow. The terms $\mathbf{F}_{\mathrm{H}}^{(\alpha)} = \left(F_x^{(\alpha)}, F_y^{(\alpha)}, F_z^{(\alpha)}\right)$ and $\mathbf{T}_{\mathrm{H}}^{(\alpha)} = \left(T_x^{(\alpha)}, T_y^{(\alpha)}, T_z^{(\alpha)}\right)$ are the hydrodynamic force and torque acting on the α-th primary particle. Since both stresslet and rate-of-strain tensors are symmetric and traceless, they are reduced to vectors composed of 5 elements per primary particle, $\mathbf{S}_H^{(\alpha)} = \left(S_{xx}^{(\alpha)}, S_{xy}^{(\alpha)}, S_{xz}^{(\alpha)}, S_{yz}^{(\alpha)}, S_{yy}^{(\alpha)}\right)$, $\mathbf{E}^\infty = \left(E_{xx}^\infty, E_{xy}^\infty, E_{xz}^\infty, E_{yz}^\infty, E_{yy}^\infty\right)$. Similarly to the angular velocity, the rate of strain of the undisturbed flow does not depend on spatial position in a pure shear flow and it is the same for all primary particles. The resistance matrix $[\mathcal{R}]$ has dimension $11N \times 11N$. It can be shown that $[\mathcal{R}]$ is symmetric and positive definite, and depends only on viscosity, size of the monomers and on their relative positions

[63]. This matrix is often divided in submatrices as follows:

$$[\mathcal{R}] = \begin{bmatrix} \mathcal{R}^{uF} & \mathcal{R}^{\omega F} & \mathcal{R}^{EF} \\ \mathcal{R}^{uT} & \mathcal{R}^{\omega T} & \mathcal{R}^{ET} \\ \mathcal{R}^{uS} & \mathcal{R}^{\omega S} & \mathcal{R}^{ES} \end{bmatrix} \tag{9}$$

where $\left[\mathcal{R}^{uF}\right]$ couples velocities and forces. The other submatrices are defined similarly.

As we are not interested in evaluating stresslets, the rows corresponding to such terms in Eq. (8) can be removed and the reduced system of equations becomes as follows:

$$\begin{bmatrix} R^{uF} & R^{\omega F} \\ R^{uT} & R^{\omega T} \end{bmatrix} \begin{Bmatrix} \mathbf{u} - \mathbf{u}^{\infty} \\ \boldsymbol{\omega} - \boldsymbol{\omega}^{\infty} \end{Bmatrix} = - \begin{Bmatrix} \mathbf{F}_{\mathrm{H}} \\ \mathbf{T}_{\mathrm{H}} \end{Bmatrix} + \begin{Bmatrix} R^{EF} \cdot \mathbf{E}^{\infty} \\ R^{ET} \cdot \mathbf{E}^{\infty} \end{Bmatrix} \tag{10}$$

where we have used a compact notation by defining $\mathbf{F}_{\mathrm{H}} = \left\{ \mathbf{F}_{\mathrm{H}}^{(1)}, \mathbf{F}_{\mathrm{H}}^{(2)}, \dots, \mathbf{F}_{\mathrm{H}}^{(N)} \right\}^{T}, \mathbf{u} = \left\{ \mathbf{u}^{(1)}, \mathbf{u}^{(2)}, \dots, \mathbf{u}^{(N)} \right\}^{T}$, and similarly for the other vectors.

The resistance matrix is built from two contributions. A first order multipole expansion of the rigorous expression for the fluid velocity gives the far field components of the matrix, which describe correctly the hydrodynamic interactions between primary particles that are relatively far apart. A correction based on lubrication theory is added to the far field matrix, in order to count for the near field hydrodynamic interactions between close pairs of primary particles in relative motion with each other. Due to the lubrication correction, the matrix $[\mathcal{R}]$ has terms diverging as $1/h$ and $\log(1/h)$ where h is the surface-to-surface distance between two primary particles, giving rise to infinitely large forces when they get in contact. However, lubrication theory assumes perfectly smooth particles in the continuum limit, and may be not representative of a colloidal suspension in which particles frequently present a finite surface roughness, where medium immobilization phenomena may limit lubrication effects. In order to mimic this condition, we introduced a *cut-off length scale* δ to regularize the singularities [64–66]: when the adimensionalized gap h/a between two approaching particles becomes lower than δ, the applied pair lubrication correc-

14

tion is no longer updated, but kept evaluated at $h = \delta a$. In the simulations we adopted $\delta = 5 \cdot 10^{-3}$.

2.2.2. Direct particle-particle interaction

In this work we assumed that direct particle-particle interactions act only as normal forces, i.e, along the center-to-center vector $\mathbf{r}_{\alpha\beta} = \mathbf{r}_\alpha - \mathbf{r}_\beta$, with $\mathbf{r}_\alpha$ and $\mathbf{r}_\beta$ being the vectors pointing to the centers of the primary particles α and β. Therefore neither a torque nor a tangential force hinders the relative rolling and sliding displacements of attached primary particles [67, 68].

The total colloidal interaction force, F_{coll}, is plotted in Figure 5 as a function of the surface-to-surface distance h normalized by the primary particle radius a. Positive values of F_{coll} correspond to a repulsive force, negative values to attraction. The gap distance h is defined as $h = r - 2a$, where r is the center-center distance between the two particles. As it can be noticed in the figure, our model is composed by two distinct curves and includes a hysteresis in order to properly describe the complex contact-detachment dynamics occurring in the presence of large adhesion forces.

[Figure 5 about here.]

When the particles are not touching each other, the usual expression for the van der Waals attraction between spheres was employed. In this case h is the actual surface-to-surface distance between the spheres. For approaching particles such a condition holds until $h = 0$, when the contact is established.

The behaviour of pairs of contacting particles is instead described by the contact mechanics theory by Johnson, Kendall and Roberts (JKR) [69], which takes into account both van der Waals and elastic interactions. In this case the gap distance h can take on negative values, because of the deformation of the contacting surfaces. Indeed, the condition of equilibrium h_{eq} corresponds to a slight overlap between the two particles, where elastic repulsion balances van der Waals attraction. When two contacting particles are pulled apart, due to the large cohesion, the contact is preserved up to a positive surface-to-

15

surface distance, referred to as pull-off distance (h_{po}), where detachment occurs abruptly. In physical terms it means that, while particles are moving apart, a small neck of material is present at the contact, preventing detachment as long as its length is smaller than h_{po}.

Non contacting particles: pure van der Waals attraction. The van der Waals attraction was calculated according to [70]:

$$F_{\mathrm{vdW}} = \frac{A_{\mathrm{H}} \cdot a}{12 \cdot (h + \ell_0)^2} \cdot f(h) \tag{11}$$

where A_{H} is the composite Hamaker constant for the interaction of two solids immersed in a third medium, and ℓ_0 is the minimum approach distance; this distance, assumed to be in the order of few Angstroms, can be thought of as the typical molecular roughness length scale of the particle surface and results from the effects of the very short-ranged intermolecular repulsive forces. The term, $f(h)$ takes into account the steeper decrease of the total interaction that occurs at large separation due to the retardation effect [71]. This effect was modeled according to [72]:

$$f(h) = \begin{cases} \dfrac{1 + 3.54p}{(1 + 1.77p^2)} & 0 < p < p_0 \\[4mm] \dfrac{0.98}{p} - \dfrac{0.434}{p^2} + \dfrac{0.067429}{p^3} & p_0 < p < \infty \end{cases} \tag{12}$$

where $p = 2\pi(h + \ell_0)/\lambda$, with λ being the London wavelength, corresponding to the intrinsic oscillations of the atoms. According to Wiese and Healy [73], the value of p_0 can be chosen in the range between 0.5 and 2.0. In order to ensure continuity of F_{vdW} we prescribed $p_0 = 0.5709$.

Contacting particles: JKR theory. The joint effect of adhesive forces and elastic response of the material after contact was modelled according to the JKR theory. For a pair of contacting particles the relationship between the force, F_{JKR}, and the surface-to-surface distance, h, is as follows:

$$h = \frac{b_0^2}{a} \left(\frac{1 + \sqrt{1 + F_{\mathrm{JKR}}/F_{\mathrm{adh}}}}{2} \right)^{1/3} \cdot \left(\frac{1 - 3\sqrt{1 + F_{\mathrm{JKR}}/F_{\mathrm{adh}}}}{3} \right), \tag{13}$$

16

where the zero-load contact radius is $b_0 = \left(9\pi\gamma_s a^2 \left(1 - \nu^2\right) / 2E\right)^{1/3}$, with γ_s being the surface energy of the solid and where ν and E are respectively the Poisson ratio and the elastic modulus of the primary particles. The adhesive force of the contact, i.e., the largest traction force that the contact can bear, is given by:

$$F_{\mathrm{adh}} = \frac{3}{2}\pi\gamma_s a \tag{14}$$

When the adhesive force is exceeded detachment takes place at a pull-off distance h given by:

$$h_{\mathrm{po}} = \left(\frac{3\pi^2\gamma_s^2 a \left(1 - \nu^2\right)^2}{8E^2}\right)^{1/3} \tag{15}$$

2.2.3. Dynamics of an encounter

Newton's equation of motion for an α-th primary particle reads as:

$$\begin{cases} m\dfrac{d\mathbf{u}^{(\alpha)}}{dt} = \mathbf{F}_{\mathrm{H}}^{(\alpha)} + \mathbf{F}_{\mathrm{coll}}^{(\alpha)} \\ I\dfrac{d\boldsymbol{\omega}^{(\alpha)}}{dt} = \mathbf{T}_{\mathrm{H}}^{(\alpha)} + \mathbf{T}_{\mathrm{coll}}^{(\alpha)} \end{cases} \tag{16}$$

where m and I are the mass and the moment of inertia of the primary particle, $\mathbf{F}^{(\alpha)}$ and $\mathbf{T}^{(\alpha)}$ the force and torque acting on it, and $\mathbf{u}^{(\alpha)}$ and $\boldsymbol{\omega}^{(\alpha)}$ its translational and angular velocity. For colloidal particles the inertial effects are generally negligible compared to the other involved forces and, consequently, Eq. (16) can be simplified as:

$$\begin{cases} \mathbf{F}_{\mathrm{H}}^{(\alpha)} = -\mathbf{F}_{\mathrm{coll}}^{(\alpha)} \\ \mathbf{T}_{\mathrm{H}}^{(\alpha)} = -\mathbf{T}_{\mathrm{coll}}^{(\alpha)} \end{cases} \tag{17}$$

The substitution of the above relationship in Eq. (10) provides the equation of motion for all the primary particles:

$$\begin{bmatrix} R^{uF} & R^{\omega F} \\ R^{uT} & R^{\omega T} \end{bmatrix} \begin{Bmatrix} \mathbf{u} - \mathbf{u}^\infty \\ \boldsymbol{\omega} - \boldsymbol{\omega}^\infty \end{Bmatrix} = \begin{Bmatrix} \mathbf{F}^{\mathrm{coll}} \\ \mathbf{T}^{\mathrm{coll}} \end{Bmatrix} + \begin{Bmatrix} R^{EF} \cdot \mathbf{E}^\infty \\ R^{ET} \cdot \mathbf{E}^\infty \end{Bmatrix} \tag{18}$$

Equation (18) is a linear system of algebraic equations that allows the calculation of $\mathbf{u} - \mathbf{u}^\infty$ and $\boldsymbol{\omega} - \boldsymbol{\omega}^\infty$ from the instantaneous spatial arrangement of the primary

particles, which determines both the resistance matrix and the direct particle-particle interactions. Finally, the trajectories of the particles are obtained from velocities by an explicit Euler integration scheme:

$$\mathbf{r}(t + \Delta t) = \mathbf{r}(t) + \mathbf{u}(t) \cdot \Delta t \tag{19}$$

The length of the time step Δt is a critical choice for the simulation, because of the steep variation of the forces acting on close primary particles. A too long time step can easily generate numerical interpenetration of the particles or, in general, unphysical behaviour. Conversely, if the time step is too small, the simulation becomes exceedingly slow. In this work an adaptive scheme was adopted for the choice of the integration step. At every iteration, we identified all the pairs of close but non-contacting monomers. Then, we set the timestep as $\Delta t = \min\left(\Delta t_b, \Delta t_{\text{opt}}\right)$, in which Δt_b is a time step base value and Δt_{opt} is the minimum of the optimal values estimated for all the close pairs of particles (α,β) as:

$$\Delta t_{\text{opt}}^{\alpha,\beta} = \begin{cases} \dfrac{0.02\ell_0}{|\mathbf{u}_\alpha - \mathbf{u}_\beta|} & \text{if} \quad h < 10\ell_0 \\ \dfrac{0.5\ell_0}{|\mathbf{u}_\alpha - \mathbf{u}_\beta|} & \text{if} \quad h < 100\ell_0 \\ \dfrac{5\ell_0}{|\mathbf{u}_\alpha - \mathbf{u}_\beta|} & \text{otherwise} \end{cases} \tag{20}$$

By this criterion we ensure that, in a single time step, two close non-contacting particles may approach at most of $0.02\ell_0$ if their gap distance is smaller than $10\ell_0$, $0.5\ell_0$ if $h < 100\ell_0$ and $5\ell_0$ otherwise. The base value Δt_b is instead used either when no pair of close particles is present or when Δt_{opt} becomes very large because $\mathbf{u}_\alpha \approx \mathbf{u}_\beta$. In this way we can reproduce accurately all the near-contact effects and safely adopt a longer timestep when monomers are far apart.

An encounter has to be simulated for a time long enough to allow the aggregates to approach from their initial position, pass by or collide, and either reach a stable configuration, through the rearrangement of the primary particles, or undergo breakup. This time was estimated on the basis of the undisturbed flow field as:

$$t_{\text{sim}} = \frac{|z_j^0|}{\dot{\gamma} y_j^0} + \frac{4\pi N_{\text{rot}}}{\dot{\gamma}} \tag{21}$$

18

where the first contribution is the time required for aggregate j to travel the distance $|z_j^0|$ and collide with aggregate i, whereas the second term is the time needed by the aggregate generated upon collision to perform N_{rot} rotations, assuming an angular velocity of $\dot{\gamma}/2$. For aggregates with dense structures, such as those simulated here, it has been reported that 8 rotations are enough to allow the aggregates to rearrange their internal structure or eventually to break up [74].

3. Results and discussion

The aim of the combined Monte Carlo - DEM approach is to predict the evolution of a colloidal suspension under the effect of a shear flow field. The simulations were conducted starting from a monodisperse population composed by spherical primary particles with radius equal to 500 nm dispersed in a suspension with solid volume fraction $\phi = 10^{-4}$. At such a small volume fraction it is reasonable to assume that each encounter involves two aggregates only. The simulation was started with 200 primary particles and the sample volume ΔV of the suspension was set in such a way to give the prescribed solid volume fraction ϕ. During the simulation, whenever the number of particles in the system fell below 150 because of aggregation, the sample volume and the population of particles were doubled, in order to keep a statistically significant number of particles in the system.

[Table 1 about here.]

In the different simulations the viscosity of the dispersing medium was varied in the range 75-100 cP, while the shear rate was kept fixed at $\dot{\gamma} = 10^4$ s^{-1}. At room temperature these conditions give Péclet numbers larger than 10^5, making the effects of Brownian motion negligible. The values of all the variables of the simulation are reported in Table 1. The magnitude of the elastic properties of the solid (elastic modulus and Poisson ratio) are typical of relatively compliant polymeric materials, such as polystyrene. Similarly, the values of the Hamaker

19

constant and surface energy are typical of polymeric particles dispersed in a liquid medium.

3.1. Dynamics of the population and size change

The main consequence of aggregation and breakup in a suspension is the variation of the size of the aggregates. For our suspensions this effect is shown in Figure 6. Graph (a) shows the evolution over time of the mean size $\langle P \rangle$ of the aggregates for different values of the shear stress $\mu\dot{\gamma}$. In this case, the size of an aggregate i is quantified by the number of constituent primary particles, P_i, and the mean size is the arithmetic average of P_i over the whole population. The behaviour at the lower stresses (750 and 875 Pa) is typical of a suspension stirred under a moderate shear rate. In the initial stages of the process the role of breakup is negligible and the evolution of the suspension is determined solely by aggregation. The initial slope of the curve, when aggregation occurs exclusively between primary particles, is related to the collision efficiency η_{11} according to:

$$\left.\frac{\mathrm{d}\langle P \rangle}{\mathrm{d}t}\right|_{t=0} = \frac{4}{\pi}\eta_{11}\phi\dot{\gamma} \qquad (22)$$

and, as shown in the inset of Figure 6a, it can be predicted quantitatively by using the expression by van de Ven and Mason for the aggregation efficiency of spherical particles:

$$\eta_{11} = f \cdot \left(\frac{A_H}{36\pi\mu\dot{\gamma}a^3}\right)^{0.18} \qquad (23)$$

where the parameter f is around 0.95 for polymeric particles of 500 nm [75].

[Figure 6 about here.]

The collision efficiency is small for the examined conditions of high shear stress: η_{11} is 0.078 for 750 Pa and 0.076 for 875 Pa, according to Eq. (23). Such
a situation is related to the intense hydrodynamic interaction between approaching particles, which induces a significant deflection of the particle trajectories and reduces the aggregation efficiency.

Since the collision rate is proportional to the cube of the particle linear size, the generation of the first aggregates in the aggregation-driven regime

20

leads to an increase of the rate of size enlargement, as clearly visible from the curves at 750 and 875 Pa. However, this condition of accelerated aggregation is rapidly dampened when some aggregates become large enough to undergo breakup. As the process proceeds, the role of breakup becomes more important and eventually an asymptotic dynamic steady state condition is reached, as a consequence of a balance between aggregation and breakup. The average size is continuously fluctuating in this regime, due to the random statistical succession of aggregation and breakup events. Some fluctuations of the average size can be already observed even in the accelerated growth region, and they can be explained as the consequence of occasional breakage events of the largest aggregates.

Breakup affects in a more substantial way the suspensions subject to larger shear stresses, in which some aggregates undergo rupture even in the initial part of the process and the accelerated aggregation stage is not present, as apparent from the curve at $\dot{\gamma} = 1000$ Pa. An additional effect of the larger shear stress is the decrease of the asymptotic size at equilibrium. Larger stresses are in fact responsible for an increase of the breakage probability, thus producing a larger number of aggregates at the equilibrium state, which are composed on average by a smaller number of primary particles. This is in line with what reported both in numerical and experimental studies where breakup of aggregates was seen to prevail over aggregation at increasing imposed shear rate [1, 9, 38].

Figure 6b reports the average size of the aggregates in terms of Sauter diameter. This average dimension characterizes the volume to surface ratio of the population and it is defined as:

$$d_{32} = 2 \cdot \frac{\sum_{i=1}^{N_a} R_i^3}{\sum_{i=1}^{N_a} R_i^2} \tag{24}$$

In comparison to $\langle P \rangle$, the Sauter diameter exhibits larger fluctuations in time. This is mostly due to the sensitivity of d_{32} to the larger aggregates of the distribution, whose concentration is relatively small and may oscillate significantly in time, but it is also a consequence of the continuous deformation experienced by aggregates; at the end of any DEM simulation, even if a missed collision

21

occurred, the aggregates may show a different shape because of the partial re-arrangement of the primary particles in the structure, and consequently have a different outer radius.

[Figure 7 about here.]

Figure 7 compares the time change of the standard deviation σ_p of the particle size distribution with the average particle size for $\mu\dot{\gamma} = 1000$ Pa. In the first stages of the process σ_P is small, since the population is made mostly of primary particles and, to a lesser extent, by small aggregates. As aggregation proceeds and larger particles are formed, σ_P increases, passes through a maximum, and eventually reaches a stationary value at around 60% of the average particle size. As clear from the plot, this asymptotic condition is attained more or less simultaneously both in the average size and in the standard deviation. The full particle size distribution for the population subject to the viscous stress of 1000 Pa sampled at $t = 283$ s (i.e., after reaching the steady state condition) is shown in Figure 8 in terms of both number of primary particles P (graph a) and outer radius R (graph b) of the aggregates. It can be seen that a significant fraction of isolated primary particles is still present at the steady state, while the remaining part of the distribution (i.e., the part related to the aggregates) resembles a log-normal curve. These features of the particle size distribution were observed at all the examined viscous stresses, but the suspensions subject to lower shear stresses showed smaller amounts of isolated primary particles and a more dispersed size distribution for the aggregates, characterized by a longer tail.

[Figure 8 about here.]

3.2. Morphology

A direct visual impression of the features of the aggregates is provided by Table 2, which reports the geometries and the main properties of a small sample of aggregates from the population stirred at 750 Pa. All aggregates are typically

22

[Table 2 about here.]

The size of colloidal aggregates is frequently characterized by means of their gyration radius R_g. The gyration radius corresponds to the root-mean-square distance of the primary particles from the center of mass of the aggregate and for an aggregate composed by P primary particles reads as:

$$R_g = \sqrt{\frac{1}{P} \sum_{\alpha}^{P} |\mathbf{r}_\alpha - \mathbf{r}_{\mathrm{cm}}|^2} \tag{25}$$

where $\mathbf{r}_\alpha$ is the position vector of the α-th primary particle and $\mathbf{r}_{\mathrm{cm}}$ identifies the location of the center of mass of the aggregate. We attempted to relate the gyration radius to the number of constituent primary particles by means of a power law of the following kind:

$$P = k_g \cdot (R_g/a)^{d_g} \tag{26}$$

where the two fitting parameters are the pre-factor k_g and the size exponent d_g. Figure 9 shows the pairs $(R_g/a, P)$ of the aggregates of the suspension sheared at $\mu \dot{\gamma} = 1000$ Pa. The regression of the data, performed by considering only clusters with $P > 3$, returned $k_g = 3.34$ and $d_g = 1.68$.

[Figure 9 about here.]

The inset of Figure 9 shows the variation over time of d_g. The large fluctuations of d_g are due to birth, death and restructuring of aggregates. However, in spite of the large fluctuations, the trend is clear: initially the value of d_g is quite large (around 2.1), then it decreases and finally attains an asymptotic value between 1.6 and 1.7 at the dynamic steady state. If the mass-size relationship is described in terms of the outer radius instead of the gyration radius, a power-law is again retrieved, $P = k_o(R/a)^{d_o}$, but the exponent d_o is slightly

23

smaller than d_g, with a starting value around 1.9 and a final asymptotic value ranging between 1.5 and 1.6.

[Figure 10 about here.]

A power law for the mass-size relationship is often assumed as an indication of a fractal structure of the aggregates and the size exponent is regarded in this context as a fractal dimension. For fractal aggregates, values smaller than 2 of the exponent correspond to highly porous structures that become more and more tenuous as size increases. However, this interpretation is valid only if the clusters are rigid and capable of creating structures that are statistically isotropic in space. On the contrary, aggregates, composed by primary particles interacting solely by central colloidal forces, such as the ones here simulated, typically show very dense structures with high coordination number [47, 76]. Therefore, the low value of the power law exponent here observed reflects a gradual transition of shape, which is approximately spheroidal for the smallest aggregates and becomes, on the average, more and more elongated as the size increases. To make this point more clear, Figure 10 compares three different aggregates of increasing size and aspect ratio sampled from the population sheared at 750 Pa and 1000 Pa. For the sake of simplicity, here we use the outer radius as characteristic size and the corresponding sphere as characteristic volume of the aggregate, but similar considerations hold for the radius of gyration as well. It is immediately apparent that, because of the increasing elongation, the solid fraction in the spherical volume decreases with size. The nearly spherical aggregates (a) and (d) fill almost completely the sphere of outer radius, whereas aggregates (c) and (f) occupy only a small portion of it. It is this feature that is captured by the small exponent of the power law, which indeed implies that the solid fraction ϕ decreases with the size of the spherical volume as $\phi \propto (R/a)^{d_o - 3}$. Therefore, the decrease of the power law exponent with time during the aggregation process reflects the dynamics of the population: in the initial part of the process the population is composed mainly of small aggregates, whose shape is almost spherical, thus determining the large

24

value of the exponent. As aggregation proceeds and larger aggregates appear, the shapes become more differentiated and the value of the exponent reduces. Thus, finally, the small solid density predicted by the mass-size power law for large clusters is a fictitious effect due to the inadequacy of a single size variable (the radius) to describe structures that may extend anisotropically in the different directions of space.

[Figure 11 about here.]

A method to better take into account the actual shape of an aggregate is to approximate its structure with an inertia equivalent ellipsoid [46, 77, 78], i.e., a triaxial ellipsoid with the same principal moments of inertia as the aggregate (Figure 10). It can be seen in fact that by using the inertia equivalent ellipsoid as a descriptor of the volume filled by the aggregate, the obtained solid fraction becomes nearly independent of the aggregate size, as made in apparent in Figure 11 where the solid fraction is estimated by using both the sphere of same outer radius and the inertia equivalent ellipsoid.

The length of the semi-axis of the inertia equivalent ellipsoid can be also used to characterize the departure of the aggregates from the spherical shape. We define the aspect ratio ($A.R.$) of an aggregate as:

$$A.R. = \frac{2a_1}{a_2 + a_3} \tag{27}$$

where a_1, a_2, a_3 are the semi-axis of the inertia equivalent ellipsoid, ordered according to decreasing magnitude ($a_1 > a_2 > a_3$). Values of $A.R.$ close to 1 indicate aggregates with a sphere-like structure, whereas larger values are an indicator of a rod-like structure. The distribution of the aspect ratio for the asymptotic population at $\mu\dot{\gamma} = 1000$ Pa is shown in Figure 12a, in which only aggregates made by a number of particles $P > 2$ were included; the amount of aggregates that show a well-defined rod structure ($A.R. > 2.50$) is significant, although most aggregates exhibit only a slightly elongated structure ($1.25 < A.R. < 2.00$). This variability of the $A.R.$ well compares with the one observed experimentally by image analysis [9, 79], confirming that, as pointed

25

[Figure 12 about here.]

The relationship between aspect ratio and size of the aggregates is shown in ₅₂₀ Figure 12b. The aspect ratio lies between a minimum value, which is around 1.2 and nearly independent of cluster size, and a maximum that increases linearly with cluster size. This implies that while the smallest aggregates are inevitably spheroidal, the largest ones show a variety of shapes, from spheroidal to highly elongated ones, with the maximum attained aspect ratio increasing with size. ₅₂₅ Spherical aggregates are usually a product of extensive internal rearrangement induced by the viscous stress. As the aggregation proceeds, spherical structures become less frequent in the population as they aggregate to form larger aggregates. In such events, restructuring phenomena in the newly generated aggregate are generally limited to the contact zone. Therefore, the obtained aggregate ₅₃₀ still presents a compact primary particle packing, but the overall shape is usually elongated.

[Figure 13 about here.]

An additional relevant characterization of colloidal aggregates is given by the density of intermonomer bonds; the number of bonds provides a measure of ₅₃₅ the local compactness of the cluster structure and therefore gives information on its resistance to disruptive stresses. In tenuous aggregates most primary particles belong to a branch of the aggregate and have two bonds only (exceptions are the terminal particles of the branches, with a single bond, and the internal particles acting as a junction between different branches, with three or more ₅₄₀ bonds). In compact clusters the number of bonds that each spherical particle forms can reach much higher values, attaining its maximum (=12) for hexagonal close packed and cubic close packed structures [44]. Figure 13 illustrates the relationship between the number of primary particles P in a cluster and its

26

mean coordination number $\bar{n}_c = 2n_b/P$, with n_b being the number of contacts

detected in the structure. It is apparent that the aggregates are compact and highly-coordinated, even if no ordered lattice was observed. This relatively large coordination number of the aggregates is due to the absence of interactions that prevent mutual sliding and rolling of the primary particles, and make the aggregates to attain a close packing as a consequence of the internal rearrangement. The average coordination number increases with the size of the cluster and it is between 5 and 6 for aggregates made of more than 15 primary particles. It should be noted however that in small clusters most of the particles are located on the outer surface, exposed to the dispersing medium and thus have a smaller number of contacts. On the contrary, in large clusters, the amount of particles at the surface is quite small in comparison with the number of particles sitting in the inner region. These particles clearly form a larger number of bonds and are responsible for the greater value of $\bar{n}_c$.

3.3. Mechanism of breakup

The stability of an aggregate in a moving fluid is determined by a balance between the cohesive forces acting between the constituent primary particles and the disruptive forces due to the hydrodynamic shear stresses exerted by the dispersing medium. The stresses discharged by the fluid onto the aggregate become more and more intense as its size increases, until a critical size is reached at which the network of internal bonds in the aggregate is no longer able to withstand the hydrodynamic stress and the aggregate splits into fragments [50, 51, 74, 81]. The fragmentation process is extremely rapid and occurs as soon as the aggregate exceeds the critical dimension following an aggregation event. A realization of such a process is shown in Figure 14 (the video of the sequence is available in the Supporting Material), where five subsequent snapshots of such an event are shown: following the approach (images *a* and *b*) and the collision of two subcritical aggregates, an aggregate of supercritical size is formed (image *c*). As soon as the aggregate aligns with the direction of greatest elongation of the flow field, the tensile forces generated by the hydrodynamic stress on the

27

aggregate become so intense that the aggregate breaks up into three fragments (image d), which are then dispersed by the shear flow (image e). In some cases it is not even necessary that a mechanical contact is made between two subcritical aggregates to induce breakage, but a very close passage is sufficient. In such cases, the mutually induced hydrodynamic may induce stresses in the aggregate structure which may overcome the internal resistance. An example is shown in the second video of the Supporting Material. Similar breakup events induced by the encounter between pair of aggregates have been discussed in recent works in which DNS-DEM simulations revealed that aggregates upon collision may bounce, with an exchange of primary particles, or may undergo breakup in two or more fragments if the aggregate generated upon collision exceeds a critical threshold size [48, 49].

[Figure 14 about here.]

[Figure 15 about here.]

As already discussed, the size of the aggregates at the steady state varies significantly with the intensity of the applied shear stress: the more intense the stress, the smaller is the mean size $\langle P \rangle$ of the aggregates in the suspension, as made apparent in Figure 15. The figure also shows the relationship between the aggregate size just before the collision leading to a breakage, $\bar{P}_{br}$, and the fluid stress $\mu\dot{\gamma}$. The value of $\bar{P}_{br}$ can be considered as an estimate of the critical size and, in accordance with the findings of several authors, it follows approximately a power law with respect to the applied stress, $\bar{P}_{br} \propto (\mu\dot{\gamma})^{-q}$, where the breakup exponent q is around 2.0 in our case. Such a value is rather high compared to the results for fractal aggregates with $d_g = 1.8$ [50], but it is instead comparable with the values obtained for more compact aggregates [82, 83]. The intensity of the hydrodynamic stress that an aggregate is able to sustain is strongly related to its shape and the significant scatter of data shown by the error bars is related to the difference in morphology of the clusters, since in the suspensions round-shaped aggregates coexist along with rod-shaped ones. For the latter class of

28

aggregates the accumulation of stresses in the internal network of bonds is much more intense and it is responsible for an increase of the breakage probability. On the other hand, round-shaped clusters have been proven to be stronger and less prone to undergo breakage [84].

It has to be remarked that the mean asymptotic size $\langle P \rangle$ is the average dimension of the population and not the critical size that separates stable aggregates from clusters undergoing rupture. The mean asymptotic cluster size is always significantly smaller than the critical size, but the decay exponent (i.e., the slope of the curve in the bilogarithmic diagram) is similar. It is therefore reasonable to infer the breaking properties of the suspension from the examination of the average size of the population, as it is often done in experimental tests.

[Figure 16 about here.]

Figure 16 reports the size distribution of the largest fragment generated upon breakup as a fraction of the size of the parent aggregate. From the data it can be seen that both fragmentation, i.e., the rupture into fragments of comparable size, and erosion, i.e., the generation of small elements from the surface of the aggregate take place. However, fragmentation is the prevailing mode of rupture and, in fact, in more than 80% of the events the size of the larger fragment is between 45% and 75% of that of the parent aggregates, with a peak around 60%. Erosion is less frequent, but a peak for fragments with size between 90% and 95% of the parent aggregates is clearly visible.

4. Conclusions

We investigated numerically the shear-induced aggregation and breakup phenomena occurring in dilute colloidal suspensions. The model was based on a mixed Monte Carlo-Discrete Element Method (DEM) approach; such a combination allowed us to dynamically simulate the behavior of a large population of colloidal aggregates in a fully predictive way. The Monte Carlo algorithm was

29

set up to sample statistically a sequence of binary encounter events between the clusters composing the population, whereas the DEM, built in the framework of Stokesian dynamics, was used to ascertain accurately the outcome of each event. In the simulation of dilute colloidal suspensions, where the simultaneous

₆₃₅ interactions between more than two aggregates are negligible, the method offers obvious advantages in comparison to a full simulation of the suspension. The reduced complexity of the calculation made it possible to include accurate evaluation of the fluid dynamic interaction (based on Stokesian dynamics), which affects significantly the stress distribution in the aggregates and their behavior

₆₄₀ in the process of aggregation and breakup.

The method was applied to the study of the dynamics of a suspension made originally of monodisperse primary particles and subject to uniform shear stresses. The suspensions studied were all characterized by a volume solid fraction equal to 10^{-4}, with a primary particle radius equal to 500 nm. The shear

₆₄₅ rate applied was equal to 10^4 s^{-1} and the viscosity of the suspending medium was varied in the range 75-100 cP, resulting at room temperature in a Péclet number approximately equal to $5 \cdot 10^5$. Primary particles were assumed to interact solely by means of central forces and therefore were free to slide and roll over each other at contact. In mild stress conditions the evolution of the suspension

₆₅₀ consists in a transition between two regimes: an initial growth phase, during which the gradient of the flow field induced aggregation of the primary particles, and a final equilibrium phase, in which a balance between aggregation and breakup of the clusters was observed; in this dynamic steady state a constant average size of the population of aggregates and a self preserving size distri-

₆₅₅ bution was established. During this phase the viscous shear stress exerted by the flow field on the cluster structure determined their breakup in two or more fragments. Under more severe conditions, breakup events affected the system earlier and involved smaller clusters.

The morphology of the aggregates was characterized in terms of size expo-

₆₆₀ nent, coordination number and aspect ratio. We did not observe significant differences in the local structural properties, such as solid fraction and coor-

30

dination number, depending on the applied stress. All aggregates present a compact, highly coordinate structure as a consequence of the ability of the primary particles to slide and roll over each other to arrange in a stable, closely packed structure.

Regarding the large-scale structure, the departure of the larger clusters from a spheroidal shape needs to be taken into account. A clear relationship between aspect ratio and dimension of the aggregate was found; most of the larger clusters presented an elongated structure, whereas smaller ones had a sphere-like structure. When the mass-size relationship is expressed in terms of a single characteristic length, a power law is obtained, where the small value of the size exponent (around 1.7) reflects this gradual transition of shape.

Rupture occurs mainly by generation of fragments of comparable size, whereas the erosion of small fragments from the surface of the cluster is less frequent and amounts to about the 10% of the breakup events. The presence of eroded fragments affects the particle size distribution, which consists of two separated regions at the steady state: one region is made of the very small particles (mostly monomers), whereas the other one, composed by the larger aggregates, shows approximately a lognormal shape. A power law with breakup exponent around 2.0 was found to relate the size of the clusters interested by breakup and the intensity of the shear stress. The same exponent was found to characterise the decay of the mean cluster size of the population with shear stress, showing that the breakup properties can be reasonably inferred from the examination of the average size of the population, as often done in experimental tests.

Funding

31

References

[1] V. Oles, Shear-induced aggregation and breakup of polystyrene latex particles, J. Colloid Interface Sci. 154 (1992) 351–358. `doi:10.1016/0021-9797(92)90149-G`.

[2] T. Serra, J. Colomer, X. Casamitjana, Aggregation and breakup of particles in a shear flow, J. Colloid Interface Sci. 187 (1997) 466–473. `doi:10.1006/jcis.1996.4710`.

[3] V. A. Tolpekin, M. H. G. Duits, D. van den Ende, J. Mellema, Aggregation and breakup of colloidal particle aggregates in shear flow, studied with video microscopy, Langmuir 20 (2004) 2614–2627. `doi:10.1021/la035758l`.

[4] L. Wang, D. L. Marchisio, R. D. Vigil, R. O. Fox, CFD simulation of aggregation and breakage processes in laminar Taylor-Couette flow, J. Colloid Interface Sci. 282 (2005) 380–396. `doi:10.1016/j.jcis.2004.08.127`.

[5] G. Frappier, B. S. Lartiges, S. Skali-Lami, Floc cohesive force in reversible aggregation: A Couette laminar flow investigation, Langmuir 26 (2010) 10475–10488. `doi:10.1021/la9046947`.

[6] K. A. Kusters, J. G. Wijers, D. Thoenes, Aggregation kinetics of small particles in agitated vessels, Chem. Eng. Sci. 52 (1997) 107–121. `doi:10.1016/S0009-2509(96)00375-2`.

[7] J. C. Flesch, P. T. Spicer, S. E. Pratsinis, Laminar and turbulent shear-induced flocculation of fractal aggregates, AIChE J. 45 (1999) 1114–1124. `doi:10.1002/aic.690450518`.

[8] D. L. Marchisio, M. Soos, J. Sefcik, M. Morbidelli, Role of turbulent shear rate distribution in aggregation and breakage processes, AIChE J. 52 (2006) 158–173. `doi:10.1002/aic.10614`.

[9] M. Soos, A. S. Moussa, L. Ehrl, J. Sefcik, H. Wu, M. Morbidelli, Effect of shear rate on aggregate size and morphology investigated under turbulent

32

715   conditions in stirred tank, J. Colloid Interface Sci. 319 (2008) 577–589. doi:10.1016/j.jcis.2007.12.005.

[10] G. Frungieri, M. U. Bäbler, M. Vanni, Shear-induced heteroaggregation of oppositely charged colloidal particles, Langmuir 36 (2020) 10739–10749. doi:10.1021/acs.langmuir.0c01536.

[11] L. Guérin, C. Coufort-Saudejaud, A. Liné, C. Frances, Dynamics of aggregate size and shape properties under sequenced flocculation in a turbulent Taylor-Couette reactor, J. Colloid Interface Sci. 491 (2017) 167–178. doi:10.1016/j.jcis.2016.12.042.

[12] L. Guerin, C. Frances, A. Liné, C. Coufort-Saudejaud, Fractal dimensions and morphological characteristics of aggregates formed in different physico-chemical and mechanical flocculation environments, Colloids Surf. A Physicochem. Eng. Asp. 560 (2019) 213–222. doi:10.1016/j.colsurfa.2018.10.017.

[13] S. Chen, S. Li, J. S. Marshall, Exponential scaling in early-stage agglomeration of adhesive particles in turbulence, Phys. Rev. Fluids 4 (2) (2019) 024304. doi:10.1103/PhysRevFluids.4.024304.

[14] I. Manas-Zloczower, Mixing and compounding of polymers: theory and practice, Carl Hanser Verlag, Munich, 2009.

[15] G. Frungieri, G. Boccardo, A. Buffo, D. Marchisio, H. A. Karimi-Varzaneh, M. Vanni, A CFD-DEM approach to study the breakup of fractal agglomerates in an internal mixer, Can J. Chem. Eng. 98 (2020) 1880–1892. doi:10.1002/cjce.23773.

[16] J. Vermant, M. Solomon, Flow-induced structure in colloidal suspensions, J. Phys.: Condens. Matter 17 (2005) R187–R216. doi:10.1088/0953-8984/17/4/R02.

33

[17] A. Mohraz, M. Solomon, Orientation and rupture of fractal colloidal gels during start-up of steady shear flow, J. Rheol. 49 (2005) 657–681. `doi:10.1122/1.1895799`.

[18] A. J. Krzysko, E. Nakouzi, X. Zhang, T. R. Graham, K. M. Rosso, G. K. Schenter, J. Ilavsky, I. Kuzmenko, M. G. Frith, C. F. Ivory, et al., Correlating inter-particle forces and particle shape to shear-induced aggregation/fragmentation and rheology for dilute anisotropic particle suspensions: a complementary study via capillary rheometry and in situ small and ultra-small angle X-ray scattering, J. Colloid Interface Sci. 576 (2020) 47–58. `doi:10.1016/j.jcis.2020.04.016`.

[19] J. S. Weston, J. Chun, G. Schenter, K. Weigandt, M. Zong, X. Zhang, K. M. Rosso, L. Anovitz, Connecting particle interactions to agglomerate morphology and rheology of boehmite nanocrystal suspensions, J. Colloid Interface Sci. 572 (2020) 328–339. `doi:10.1016/j.jcis.2020.03.109`.

[20] E. Gavi, D. L. Marchisio, A. A. Barresi, M. G. Olsen, R. O. Fox, Turbulent precipitation in micromixers: CFD simulation and flow field validation, Chem. Eng. Res. Des. 88 (2010) 1182–1193. `doi:10.1016/j.cherd.2010.01.025`.

[21] D. Ramkrishna, Population Balances - Theory and Applications to Particulate Systems in Engineering, Academic Press, San Diego, 2000. `doi:10.1016/B978-0-12-576970-9.X5000-0`.

[22] M. Vanni, Approximate population balance equations for aggregation-breakage processes, J. Colloid Interface Sci. 221 (2000) 143–160. `doi:10.1006/jcis.1999.6571`.

[23] D. L. Marchisio, R. D. Vigil, R. O. Fox, Implementation of the quadrature method of moments in CFD codes for aggregation-breakage problems, Chem. Eng. Sci. 58 (2003) 3337–3351. `doi:10.1016/S0009-2509(03)00211-2`.

34

[24] M. U. Bäbler, M. Morbidelli, Analysis of the aggregation-fragmentation population balance equation with application to coagulation, J. Colloid Interface Sci. 316 (2007) 428–441. `doi:10.1016/j.jcis.2007.08.029`.

[25] M. Soos, L. Wang, R. O. Fox, J. Sefcik, M. Morbidelli, Population balance modeling of aggregation and breakage in turbulent Taylor-Couette flow, J. Colloid Interface Sci. 307 (2007) 433–446. `doi:10.1016/j.jcis.2006.12.016`.

[26] R. I. Jeldres, F. Concha, P. G. Toledo, Population balance modelling of particle flocculation with attention to aggregate restructuring and permeability, Adv. Colloid Interface Sci. 224 (2015) 62–71. `doi:10.1016/j.cis.2015.07.009`.

[27] A. H. Alexopoulos, C. Kiparissides, Solution of the bivariate dynamic population balance equation in batch particulate systems: Combined aggregation and breakage, Chem. Eng. Sci. 62 (2007) 5048–5053. `doi:10.1016/j.ces.2007.01.039`.

[28] S. Lazzari, B. Jaquet, L. Colonna, G. Storti, M. Lattuada, M. Morbidelli, Interplay between aggregation and coalescence of polymeric particles: Experimental and modeling insights, Langmuir 31 (2015) 9296–9305. `doi:10.1021/acs.langmuir.5b02503`.

[29] I. Kryven, S. Lazzari, G. Storti, Population balance modeling of aggregation and coalescence in colloidal systems, Macromol. Theor. Simul. 3 (2015) 170–181. `doi:10.1002/mats.201300140`.

[30] M. Kostoglou, A. G. Konstandopoulos, Evolution of aggregate size and fractal dimension during Brownian coagulation, J. Aerosol Sci. 32 (2001) 1399–1420. `doi:10.1016/S0021-8502(01)00056-8`.

[31] M. Kostoglou, A. G. Konstandopoulos, S. K. Friedlander, Bivariate population dynamics simulation of fractal aerosol aggregate coagulation and

restructuring, J. Aerosol Sci. 37 (2006) 1102–1115. `doi:10.1016/j.jaerosci.2005.11.009`.

[32] M. U. Bäbler, L. Biferale, A. S. Lanotte, Breakup of small aggregates driven by turbulent hydrodynamical stress, Phys. Rev. E 85 (2) (2012) 025301. `doi:10.1103/PhysRevE.85.025301`.

[33] M. U. Bäbler, M. Morbidelli, J. Bałdyga, Modelling the breakup of solid aggregates in turbulent flows, J. Fluid Mech. 612 (2008) 261–289. `doi:10.1017/S002211200800298X`.

[34] A. Zaccone, M. Soos, M. Lattuada, H. Wu, M. U. Bäbler, M. Morbidelli, Breakup of dense colloidal aggregates under hydrodynamic stresses, Phys. Rev. E 79 (6) (2009) 061401. `doi:10.1103/PhysRevE.79.061401`.

[35] Y. Drossinos, A. D. Melas, M. Kostoglou, L. Isella, Morphology-dependent random binary fragmentation of in silico fractal-like agglomerates, EPL-Europhys. Lett. 127. `doi:10.1209/0295-5075/127/46002`.

[36] M. L. Eggersdorfer, D. Kadau, H. J. Herrmann, S. E. Pratsinis, Fragmentation and restructuring of soft-agglomerates under shear, J. Colloid Interface Sci. 342 (2010) 261–268. `doi:10.1016/j.jcis.2009.10.062`.

[37] M. Kroupa, M. Vonka, J. Kosek, Modeling the mechanism of coagulum formation in dispersions, Langmuir 30 (2014) 2693–2702. `doi:10.1021/la500101x`.

[38] M. Kroupa, M. Vonka, M. Soos, J. Kosek, Size and structure of clusters formed by shear induced coagulation: modeling by discrete element method, Langmuir 31 (2015) 7727–7737. `doi:10.1021/acs.langmuir.5b01046`.

[39] J. F. Wilson, M. Kroupa, J. Kosek, M. Soos, Numerical study of soft colloidal nanoparticles interaction in shear flow, Langmuir 34 (2018) 15600–15611. `doi:10.1021/acs.langmuir.8b03350`.

[40] X. Ruan, S. Chen, S. Li, Structural evolution and breakage of dense ag-
glomerates in shear flow and Taylor-Green vortex, Chem. Engi. Sci. 211
(2020) 115261. `doi:10.1016/j.ces.2019.115261`.

[41] G. Frungieri, A novel Monte Carlo - Discrete Element Method approach
for the micro-mechanics of colloidal suspensions, Ph.D. thesis, Politecnico
di Torino (2018).

[42] G. Frungieri, M. Vanni, In Dynamics of a shear-induced aggregation process
by a combined Monte Carlo-Stokesian Dynamics approach, Proceedings of
the 9th International Conference on Multiphase Flow, 22-27 May 2016,
Firenze, Italy.

[43] J.-S. Kroll-Rabotin, M. Gisselbrecht, B. Ott, R. May, J. Fröhlich, J.-P.
Bellot, Multiscale simulation of non-metallic inclusion aggregation in a fully
resolved bubble swarm in liquid steel, Metals 10 (2020) 517. `doi:10.3390/`
`met10040517`.

[44] A. Gastaldi, M. Vanni, The distribution of stresses in rigid fractal-like
aggregates in a uniform flow field, J. Colloid Interface Sci. 357 (2011) 18–
30. `doi:10.1016/j.jcis.2011.01.080`.

[45] J. De Bona, A. S. Lanotte, M. Vanni, Internal stresses and breakup of
rigid isostatic aggregates in homogeneous and isotropic turbulence, J. Fluid
Mech. 755 (2014) 365–396. `doi:10.1017/jfm.2014.421`.

[46] G. Frungieri, M. Vanni, Shear-induced aggregation of colloidal particles: A
comparison between two different approaches to the modelling of colloidal
interactions, Can. J. Chem. Eng. 95 (2017) 1768–1780. `doi:10.1002/cjce.`
`22843`.

[47] V. Becker, E. Schlauch, M. Behr, H. Briesen, Restructuring of colloidal ag-
gregates in shear flows and limitations of the free-draining approximation,
J. Colloid Interface Sci. 339 (2009) 362–372. `doi:10.1016/j.jcis.2009.`
`07.022`.

[48] F. F. Dizaji, J. S. Marshall, J. R. Grant, Collision and breakup of fractal particle agglomerates in a shear flow, J. Fluid Mech. 862 (2019) 592–623. `doi:10.1017/jfm.2018.959`.

[49] S. Chen, S. Li, Collision-induced breakage of agglomerates in homogenous isotropic turbulence laden with adhesive particles, Journal of Fluid Mechanics 902.

[50] M. Vanni, A. Gastaldi, Hydrodynamic forces and critical stresses in low-density aggregates under shear flow, Langmuir 27 (2011) 12822–12833. `doi:10.1021/la2024549`.

[51] Y. M. Harshe, M. Lattuada, Breakage rate of colloidal aggregates in shear flow through Stokesian dynamics, Langmuir 28 (2012) 283–292. `doi:10.1021/la2038476`.

[52] K. Rajamani, W. T. Pate, D. J. Kinneberg, Time-driven and event-driven Monte Carlo simulations of liquid-liquid dispersions: a comparison, Ind. Eng. Chem. Fundamen. 25 (1986) 746–752. `doi:10.1021/i100024a045`.

[53] D. Ramkrishna, Analysis of population balance – IV. The precise connection between Monte Carlo simulation and population balances, Chem. Eng. Sci. 36 (1981) 1203–1209. `doi:10.1016/0009-2509(81)85068-3`.

[54] K. Liffman, A direct simulation Monte-Carlo method for cluster coagulation, J. Comput. Phys. 100 (1992) 116–127. `doi:10.1016/0021-9991(92)90314-0`.

[55] M. von Smoluchowski, Versuch einer mathematischen Theorie der Koagulationskinetik kolloider Lösungen, Z. Phys. Chem 92 (1917) 129–168.

[56] B. H. Shah, D. Ramkrishna, J. D. Borwanker, Simulation of particulate systems using the concept of the interval of quiescence, AIChE J. 23 (1977) 897–904. `doi:10.1002/aic.690230617`.

38

[57] F. E. Kruis, A. Maisels, H. Fissan, Direct simulation Monte Carlo method for particle coagulation and aggregation, AIChE J. 46 (2000) 1735–1742. `doi:10.1002/aic.690460905`.

[58] M. Smith, T. Matsoukas, Constant-number Monte Carlo simulation of population balances, Chem. Eng. Sci. 53 (1998) 1777–1786. `doi:10.1016/S0009-2509(98)00045-1`.

[59] P. Tandon, D. E. Rosner, Monte Carlo simulation of particle aggregation and simultaneous restructuring, J. Colloid Interface Sci. 213 (1999) 273–286. `doi:10.1006/jcis.1998.6036`.

[60] K. Horii, R. Yamada, S. Harada, Strength deterioration of nonfractal particle aggregates in simple shear flow, Langmuir 31 (2015) 7909–7918. `doi:10.1021/acs.langmuir.5b00197`.

[61] L. Durlofsky, J. F. Brady, G. Bossis, Dynamic simulation of hydrodynamically interacting particles, J. Fluid Mech. 180 (1987) 21–49. `doi:10.1017/S002211208700171X`.

[62] J. F. Brady, G. Bossis, Stokesian dynamics, Annu. Rev. Fluid Mech. 20 (1988) 111–157. `doi:10.1146/annurev.fl.20.010188.000551`.

[63] S. Kim, S. J. Karrila, Microhydrodynamics: Principles and Selected Applications, Dover, 2005.

[64] R. Seto, R. Mari, J. F. Morris, M. M. Denn, Discontinuous shear thickening of frictional hard-sphere suspensions, Phys. Rev. Lett. 111 (2013) 218301. `doi:10.1103/PhysRevLett.111.218301`.

[65] M. Trulsson, B. Andreotti, P. Claudin, Transition from the viscous to inertial regime in dense suspensions, Phys. Rev. Lett. 109 (2012) 118305. `doi:10.1103/PhysRevLett.109.118305`.

[66] R. Mari, R. Seto, J. F. Morris, M. M. Denn, Shear thickening, frictionless and frictional rheologies in non-Brownian suspensions, J. Rheol. 58 (2014) 1693–1724. `doi:10.1122/1.4890747`.

[67] V. Becker, H. Briesen, Tangential-force model for interactions between bonded colloidal particles, Phys. Rev. E 78 (2008) 061404. `doi:10.1103/PhysRevE.78.061404`.

[68] J. P. Pantina, E. M. Furst, Elasticity and critical bending moment of model colloidal aggregates, Phys. Rev. Lett. 94 (2005) 138301. `doi:10.1103/PhysRevLett.94.138301`.

[69] K. L. Johnson, K. Kendall, A. D. Roberts, Surface energy and the contact of elastic solids, Proc. R. Soc. Lond. A 324 (1971) 301–313. `doi:10.1098/rspa.1971.0141`.

[70] H. C. Hamaker, The London–van der Waals attraction between spherical particles, Physica 4 (1937) 1058–1072. `doi:10.1016/S0031-8914(37)80203-7`.

[71] H. J. Butt, M. Kappl, Surface and Interfacial Forces, Wiley, 2009.

[72] M. Vanni, G. Baldi, Coagulation efficiency of colloidal particles in shear flow, Adv. Colloid Interface Sci. 97 (2002) 151–177. `doi:10.1016/S0001-8686(01)00050-1`.

[73] G. R. Wiese, T. W. Healy, Effect of particle size on colloid stability, Trans. Faraday Soc. 66 (1970) 490–499.

[74] Z. Ren, Y. M. Harshe, M. Lattuada, Influence of the potential well on the breakage rate of colloidal aggregates in simple shear and uniaxial extensional flows, Langmuir 31 (2015) 5712–5721. `doi:10.1021/la504966y`.

[75] T. G. M. van de Ven, S. G. Mason, The microrheology of colloidal dispersions VII. Orthokinetic doublet formation of spheres, Colloid Polym. Sci. 255 (5) (1976) 468–479. `doi:10.1007/BF01536463`.

[76] L. Isella, Y. Drossinos, Langevin agglomeration of nanoparticles interacting via a central potential, Phys. Rev. E 82 (2010) 011404. `doi:10.1103/PhysRevE.82.011404`.

[77] Y. M. Harshe, L. Ehrl, M. Lattuada, Hydrodynamic properties of rigid fractal aggregates of arbitrary morphology, J. Colloid Interface Sci. 352 (2010) 87–98. `doi:10.1016/j.jcis.2010.08.040`.

[78] L. Sanchez Fellay, C. Twist, M. Vanni, Motion of rigid aggregates under different flow conditions, Acta Mech. 224 (2013) 2225–2248. `doi:10.1007/s00707-013-0928-9`.

[79] S. Blaser, Flocs in shear and strain flows, J. Colloid Interface Sci. 225 (2) (2000) 273–284. `doi:10.1006/jcis.1999.6671`.

[80] C. Selomulya, R. Amal, G. Bushell, T. D. Waite, Evidence of shear rate dependence on restructuring and breakup of latex aggregates, J. Colloid Interface Sci. 236 (1) (2001) 67–77. `doi:10.1006/jcis.2000.7372`.

[81] K. Higashitani, K. Iimura, H. Sanda, Simulation of deformation and breakup of large aggregates in flows of viscous fluids, Chem. Eng. Sci. 56 (2001) 2927–2938. `doi:10.1016/S0009-2509(00)00477-2`.

[82] S. Horwatt, I. Manas-Zloczower, D. Feke, Dispersion behavior of heterogeneous agglomerates at supercritical stresses, Chem. Eng. Sci. 47 (1992) 1849–1855. `doi:10.1016/0009-2509(92)80303-T`.

[83] B. Ó Conchúir, A. Zaccone, Mechanism of flow-induced biomolecular and colloidal aggregate breakup, Phys. Rev. E 87 (2013) 032310. `doi:10.1103/PhysRevE.87.032310`.

[84] M. Vanni, Accurate modelling of flow induced stresses in rigid colloidal aggregates, Comput. Phys. Commun 192 (2015) 70–90. `doi:10.1016/j.cpc.2015.02.022`.
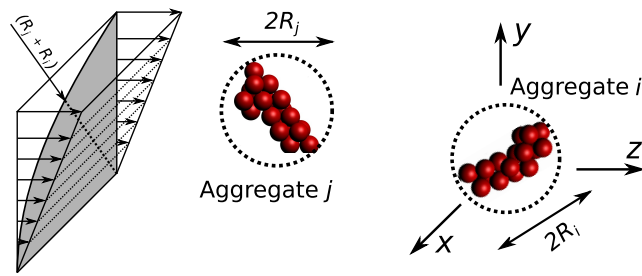
Figure 1: Schematic of an encounter between aggregates i and j in a uniform shear flow. The grey area represents a quarter of the Smoluchowski cross section for aggregates of size R_i and R_j.
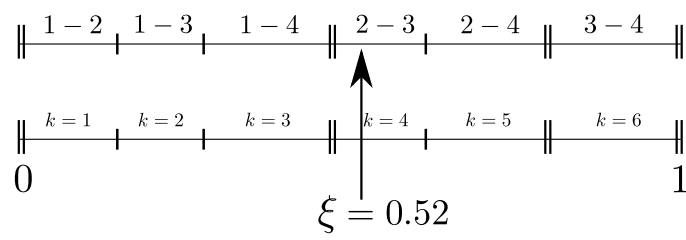
Figure 2: Representation of the ordering scheme and sampling technique for a sample population composed by 4 particles. The amplitude of each interval is proportional to the probability of encounter between the two particles. In the reported case, by picking $\xi = 0.52$ the encounter of particles 2 and 3 is sampled.
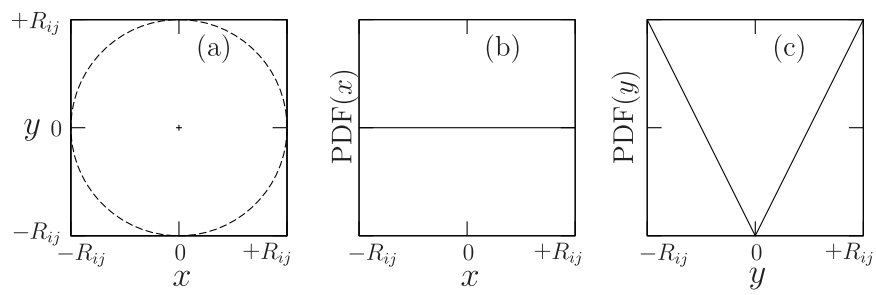
Figure 3: Encounter cross section in the $x - y$ plane (graph a) and distribution of the probability that aggregate j crosses the plane at a given x-coordinate (graph b) and y-coordinate (graph c). Here R_{ij} stands for $R_i + R_j$.
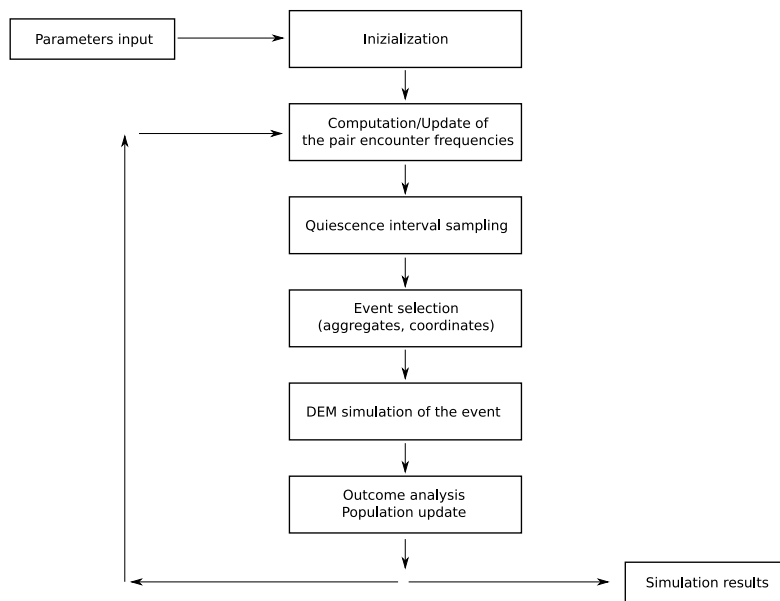
Figure 4: Flow chart of the simulation technique.
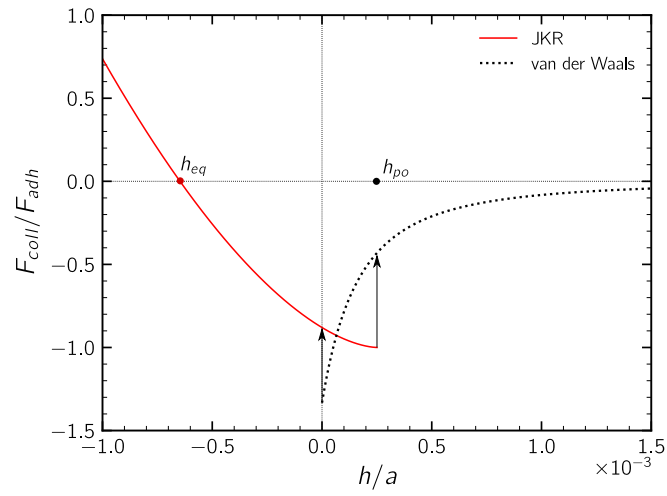
Figure 5: Colloidal interaction F_{coll} between two primary particles for the system described in Table 1. Black dotted line: van der Waals attraction ($F_{coll} = F_{vdW}$); Red solid line: JKR theory of contact mechanics ($F_{coll} = F_{JKR}$). The coordinates h_{eq} and h_{po} represent the equilibrium and the pull-off distance, respectively.
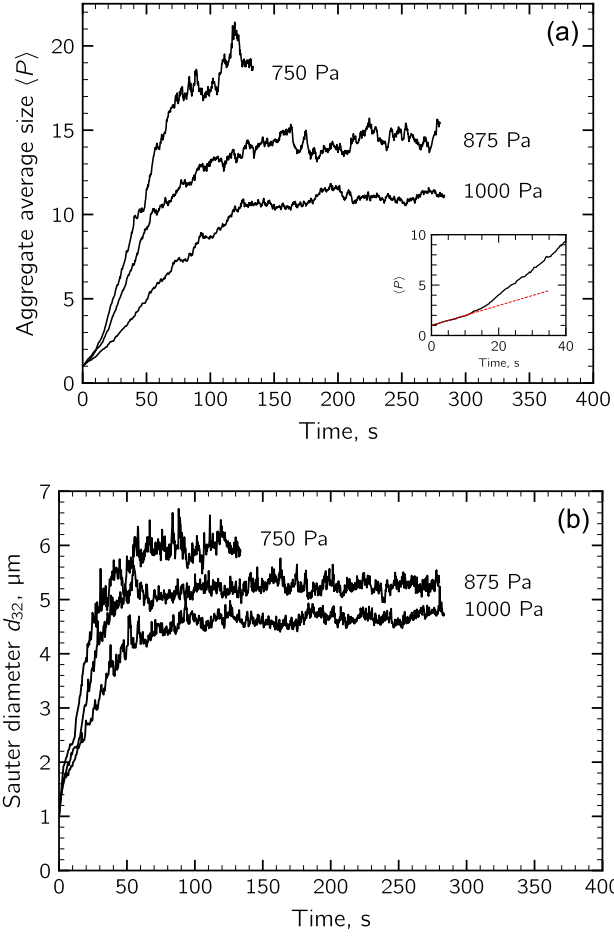
Figure 6: Time evolution of the average size of the clusters $\langle P \rangle$ (a) and mean Sauter diameter of the population d_{32} (b) for suspensions at shear stresses of $\mu\dot{\gamma} = 750, 875, 1000$ Pa. The inset in graph (a) reports the initial trend for 750 Pa and compares the simulation (continuous black line) with the initial slope predicted by Eq. (22) (red dashed line).

47
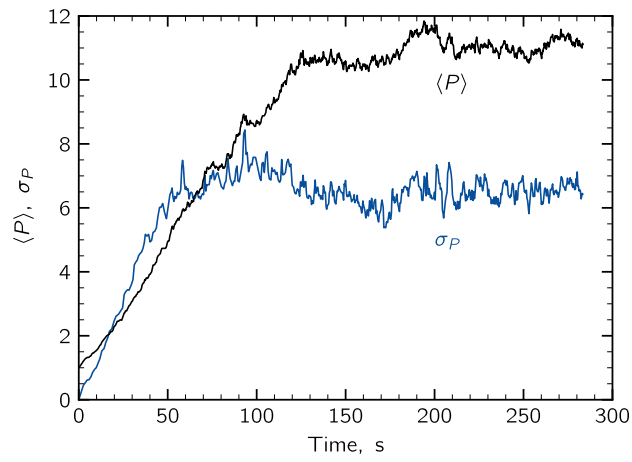
Figure 7: Average size of the clusters $\langle P \rangle$ and standard deviation of the size distribution σ_P as a function of time for $\mu\dot{\gamma}$=1000 Pa.
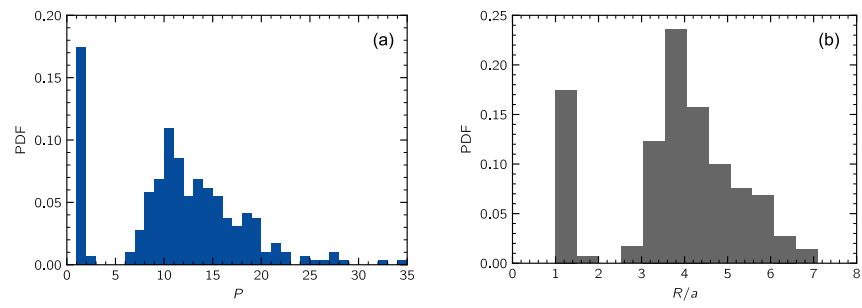
Figure 8: Particle size distribution as a function of the number of primary particles in the aggregate (a) and the outer radius of the aggregate (b) in the asymptotic steady state condition ($t = 283$ s) for $\mu\dot{\gamma} = 1000$ Pa.
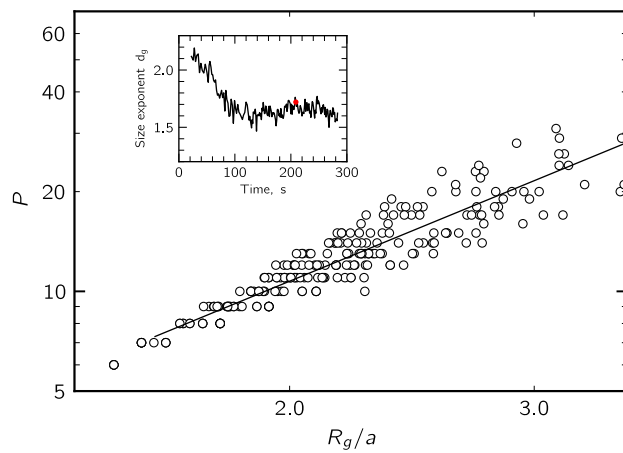
Figure 9: Power law dependence between the number of primary particles P and the gyration radius R_g of the aggregates of the suspension subject to $\mu\dot{\gamma} = 1000$ Pa. In the inset the change of the power law exponent over time is shown.
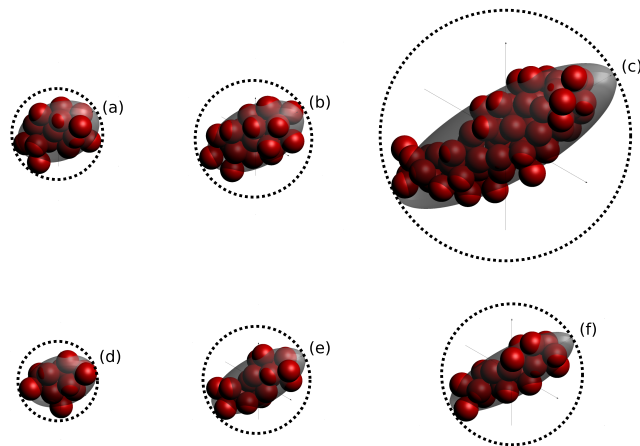
Figure 10: Clusters from the population sheared at 750 Pa (top) and 1000 Pa (bottom) and characteristic solid fraction ϕ based on the sphere of outer radius. (a) 17 monomers, $\phi = 0.18$; (b) 22 monomers, $\phi = 0.15$; (c) 64 monomers; $\phi = 0.052$, (d) 12 monomers, $\phi = 0.18$; (e) 17 monomers, $\phi = 0.11$; (f) 19 monomers, $\phi = 0.081$.
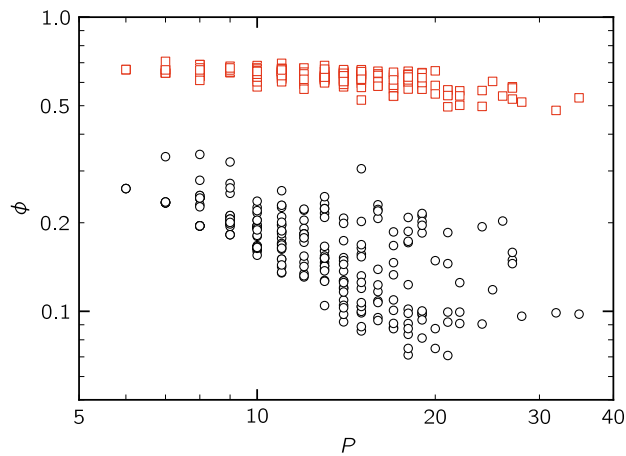
Figure 11: Solid fraction of the aggregate structures from the asymptotic population sheared at 1000 Pa for varying number of primary particles in the aggregate. The total volume is estimated as the volume of the sphere with same outer radius (black circles) and as the volume of the inertia equivalent ellipsoid (red squares).
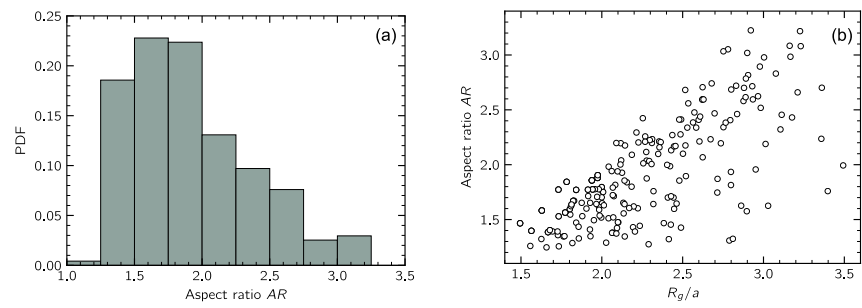
Figure 12: Aspect ratio of the steady state population of aggregates for $\mu\dot{\gamma} = 1000$ Pa. a) PDF of the aspect ratio. b) Correlation between aspect ratio and cluster size for the same population.
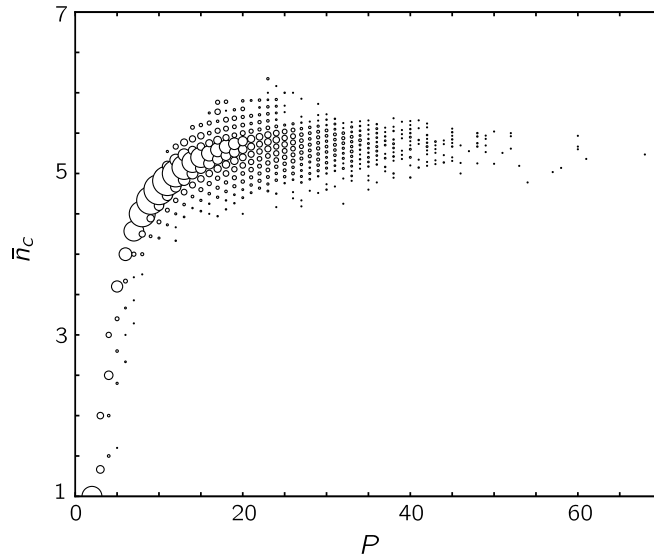
Figure 13: Relationship between the number of primary particles P and the average coordination number $\bar{n}_c$ for the aggregates of the asymptotic population sheared at $\mu\dot{\gamma} = 1000$ Pa. The size of the markers is proportional to the number of aggregates with the same $P - \bar{n}_c$ value.
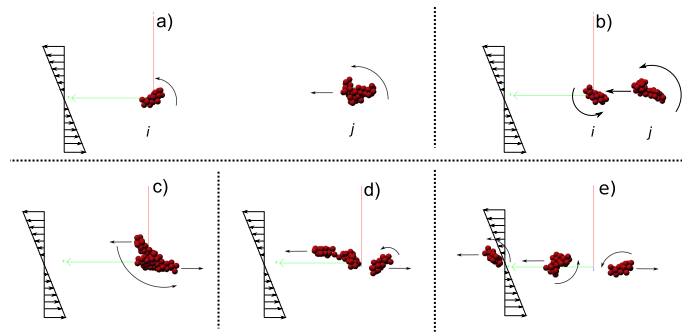
Figure 14: Snapshots of an encounter event in simple shear flow ($\mu\dot{\gamma} = 750$ Pa) leading to the breakup of the just formed aggregate. (a-b) Aggregate j moves towards aggregate i, because of the velocity gradient and initial offset. Both aggregates rotate counterclockwise; (c) immediately after their collision a supercritical aggregate is formed which continues to rotate counterclockwise; (d) the aggregate breaks into fragments as soon as the orientation of maximum stress is reached; (e) the fragments are carried away by the fluid flow. The video of the sequence is available in the Supporting Material.
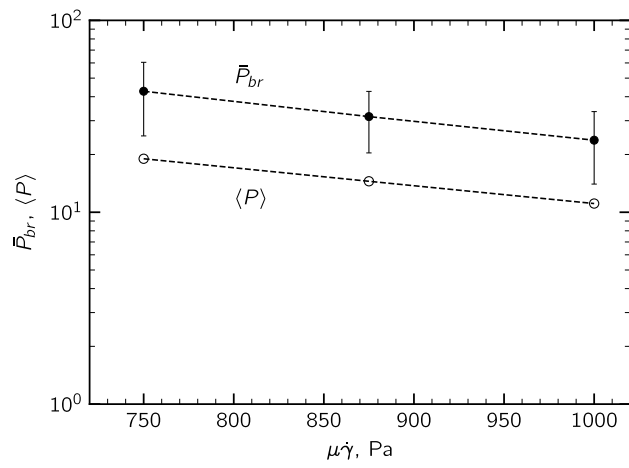
Figure 15: Average number of primary particles of the colliding clusters just before breakup $\bar{P}_{br}$ and mean aggregate size at the steady state $\langle P \rangle$ as a function of the strength of shear stress $\mu\dot{\gamma}$. Error bars indicate the standard deviation of the data.
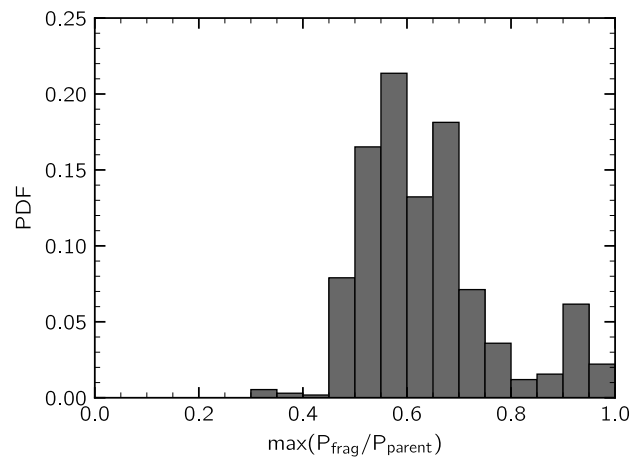
Figure 16: Distribution of the maximum fragment size generated upon breakage for $\mu\dot{\gamma} = 1000$ Pa.

Table 1: Main variables of the Monte Carlo - DEM simulations

Parameter	Symbol	Value
Volume fraction of solid	ϕ	10^{-4}
Hamaker constant	A_H	$0.97 \cdot 10^{-20}$ J
Surface energy	γ_s	$4.7 \cdot 10^{-3}$ J/m^2
Monomer radius	a	500 nm
Medium viscosity	μ	$75 - 100$ cP
Shear rate	$\dot{\gamma}$	10^4 s^{-1}
Elastic modulus	E	3.4 GPa
Poisson ratio	ν	0.5
Minimum approach distance	ℓ_0	0.165 nm
Base time-step value	Δt_b	10^{-6} s

Table 2: Geometries and main characteristics of a sample of clusters of the suspension with $\mu\dot{\gamma} = 750$ Pa at the dynamic steady state. P: number of primary particles; R_g: gyration radius; R: outer radius; $A.R.$: aspect ratio; $\bar{n}_c$: mean coordination number

Geometry	P	R_g/a	R/a	$A.R.$	$\bar{n}_c$
	21	2.76	5.08	2.25	5.43
	54	4.10	8.42	1.69	5.33
	27	3.56	7.20	2.90	5.41
	15	2.18	4.20	1.43	5.20
	15	2.28	4.16	1.38	5.20
	18	2.88	5.82	2.90	5.33
	22	2.68	4.84	1.74	5.46
	30	3.24	6.48	1.49	5.68
	29	3.34	6.84	2.44	5.59
	19	3.20	6.38	3.64	5.37